Resonance ionization spectroscopy of sodium Rydberg levels using difference frequency generation of high-repetition-rate pulsed Ti:sapphire lasers

P. Naubereit,[*] J. Marín-Sáez,[†] F. Schneider, A. Hakimi, M. Franzmann,[‡] T. Kron, S. Richter, and K. Wendt
Institute of Physics, University of Mainz, D-55128 Mainz, Germany
(Received 8 March 2016; published 31 May 2016)

The generation of tunable laser light in the green to orange spectral range has generally been a deficiency of solid-state lasers. Hence, the formalisms of difference frequency generation (DFG) and optical parametric processes are well known, but the DFG of pulsed solid-state lasers was rarely efficient enough for its use in resonance ionization spectroscopy. Difference frequency generation of high-repetition-rate Ti:sapphire lasers was demonstrated for resonance ionization of sodium by efficiently exciting the well-known D_1 and D_2 lines in the orange spectral range (both ≈ 589 nm). In order to prove the applicability of the laser system for its use at resonance ionization laser ion sources of radioactive ion beam facilities, the first ionization potential of Na was remeasured by three-step resonance ionization into Rydberg levels and investigating Rydberg convergences. A result of $E_{\mathrm{IP}} = 41449.455(6)_{\mathrm{stat}}(7)_{\mathrm{sys}}\ \mathrm{cm}^{-1}$ was obtained, which is in perfect agreement with the literature value of $E_{\mathrm{IP}}^{\mathrm{lit}} = 41449.451(2)\ \mathrm{cm}^{-1}$. A total of 41 level positions for the odd-parity Rydberg series $nf\ ^2F^{o}_{5/2,7/2}$ for principal quantum numbers of $10 \leqslant n \leqslant 60$ were determined experimentally.

DOI: 10.1103/PhysRevA.93.052518

I. INTRODUCTION

Powerful tunable high-repetition-rate solid-state lasers are a most useful tool for spectroscopy and ion production at radioactive ion beam (RIB) facilities, which use resonance ionization laser ion sources (RILIS). Those lasers may be used in long-term stable and almost maintenance-free continuous operation and, moreover, they permit a rather simple spectral range extension by generation of the second, third, or fourth harmonic. Using a titanium:sapphire crystal as active laser medium a wavelength coverage of 680 nm to 1000 nm in fundamental mode and 210 nm to 450 nm by using frequency doubling, tripling and quadrupling, has been demonstrated. Nevertheless, a remaining gap in the visible spectral range between the fundamental (> 680 nm) and the second harmonic (< 450 nm) output is remaining. The second-order nonlinear process of difference frequency generation (DFG) allows to close that gap. The theory of this process can be found for example in [1]. The desired wavelength range is also achievable with a variety of different laser systems with or without DFG. Most of them are even commercially available for many years. However, those systems do not really fulfill the requirements at on-line facilities as pointed out explicitly above. Continuous-wave laser systems, for example, operating as Raman lasers [2] or using sum frequency generation [3], are not able to provide either the high output energies or the spectral coverage needed for saturation of a broadened excitation line for a thermal atom ensemble, in particular regarding weaker atomic transitions. In contrast, high pulse energies are needed for optical parametric oscillators or amplifiers [4] and are in most cases only achieved at low repetition rates. The corresponding duty cycle losses of such low-repetition-rate operation are a huge disadvantage concerning the efficiencies of ion production at RIB facilities. Dye lasers instead can provide both high repetition rate and high pulse energies with a broad range of output wavelengths [5]. Unlike the high-repetition-rate solid-state lasers, however, dye lasers need a lot of maintenance and care during long-term operation in order to guarantee suitable performance and stability as needed at RIB facilities. The principle of the DFG approach has been demonstrated using high-repetition-rate ns Ti:sapphire lasers in [6]. In this work, the reliable application in high-resolution multistep resonance ionization spectroscopy is shown.

As an evaluation case, Rydberg spectroscopy on the element with the probably best known transitions in the orange wavelength regime around 590 nm was chosen by addressing the famous D_1 and D_2 doublet lines of sodium. By using three-step resonance ionization, involving DFG in the first excitation step, spectroscopy around the sodium ionization potential was performed and its value was redetermined. Although this value has been known with high precision since 1992 ($E_{\mathrm{IP}}^{\mathrm{lit}} = 41449.451(2)\,\mathrm{cm}^{-1}$ [7,8]), energies of higher lying levels of odd-parity Rydberg series like $nf\ ^2F^{o}_{5/2,7/2}$ were just published for the first time during the analysis of our data in 2015 by Nadeem and co-workers [9]. These authors give an elaborate overview on the atomic spectroscopy of high-lying levels of sodium, to which we refer here for a general overview. They have carried out two-color, three-step resonance excitation based upon the $3s$-$3d$ two-photon transition from the ground state and finally populate nf levels in the range $15 \leqslant n \leqslant 51$. Results include level energies and oscillator strengths. They report an uncertainty of their level energies of $0.2\,\mathrm{cm}^{-1}$ due to strong broadening effects in their thermionic diode setup, which is almost one order of magnitude less precise than the results of our measurements with in-source laser geometry on a well-collimated atomic beam. In addition, our data, resulting from three-color, three-step resonance excitation along two different excitation ladders, which were based upon the D_1 and D_2 ground-state transitions, respectively, extend to higher principal quantum numbers of up to $n = 60$. Correspondingly,

[*]naubereit@uni-mainz.de
[†]Present address: Applied Physics Section of the Environmental Department, University of Lleida, Escuela Politécnica Superior, Jaume II 69, 25001 Lleida, Spain.
[‡]Institute for Radioecology and Radiation Protection, University of Hannover, D-30419 Hannover, Germany.

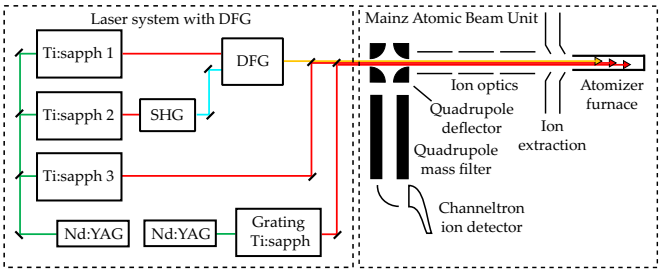

FIG. 1. Sketch of the experimental setup including the laser system and the atomic beam mass spectrometer unit MABU.

we have attempted a full Rydberg-Ritz analysis of our data including earlier known literature data as bandheads and redetermined the ionization potential with high accuracy. This approach resulted in a confirmation of the high-precision literature value of $E_{\mathrm{IP}}^{\mathrm{lit}} = 41449.451(2)\,\mathrm{cm}^{-1}$ from [7,8] in an independent measurement.

II. APPARATUS

Figure 1 gives an overview of the experimental apparatus used. It consists of two distinct components: the dedicated high-repetition-rate solid-state laser system including the DFG unit and the atomic beam apparatus with single ion detection MABU (Mainz atomic beam unit).

A. Laser system

1. General layout

For a resonant three-step ionization process involving DFG, four Ti:sapphire lasers are necessary: Two of them provide the input for the DFG, which is used for the first excitation step. The higher energetic pump wave of the DFG process is generated by frequency doubling of the fundamental laser light in a BBO crystal. The lower energetic, subtracted idler wave is provided in the fundamental infrared range of the Ti:sapphire laser. The radiation of the third laser excites the atoms in a second resonant step into the second excited state. Those three lasers are based on the standard Z-shaped cavity design of the Mainz Ti:sapphire lasers in the latest design according to [10]. The ionization step is then provided from a fourth laser, which is a grating-assisted Ti:sapphire laser [11] to guarantee a wide, continuously tunable scanning range.

To achieve sufficient pump power and temporal synchronous output pulses of the Ti:sapphire lasers, two commercial frequency-doubled Nd:YAG pump lasers with 10-kHz repetition rates (Quantronix Hawk-Pro 532-60-M and Photonics Industries DM 80-532) were used. The standard Mainz Ti:sapphire lasers provide an average power between 2 and 4 W at pump powers of 15 W. The pulse lengths span from 25 ns at the gain maximum of ≈ 810 nm to 100 ns at the edges of the tuning range around 700 and 1000 nm, respectively, whereas the spectral bandwidth amounts to typically $\Delta\nu_{\mathrm{fund}} = 4(1)$ GHz. In the experiment the grating-assisted laser had an output power of ≈ 280 mW with a bandwidth of 2 GHz. The lasers show a good long-term stability with frequency drifts of less than 1 GHz a day. Nevertheless, the wavelengths of all lasers were actively monitored during the experiment.

2. Considerations for difference frequency generation

In [6] a high-repetition-rate, pulsed, narrow-bandwidth Ti:sapphire laser involving injection locking was used for DFG. This laser has both a narrow bandwidth of 20 MHz and a suitable output power of 2.6 W. Frequency doubling was carried out in a very efficient but somewhat delicate intracavity approach. Despite some advantages of this setup, we followed a different approach here and used the standard Mainz Ti:sapphire lasers as described above to guarantee the universality of the DFG system without involving and controlling the sophisticated injection locking procedure. In addition we abstained from intracavity doubling for the DFG pump photon generation to provide a more simple frequency-tuning procedure for both the second harmonic light and the DFG light at the expense of a reduced output power. Based on calculations for optimization of the mixing process with the software SNLO [12], we expected considerable losses in the DFG process, as the different available BBO crystals had to be tilted quite far off from orthogonal orientation due to imperfect cutting angles for proper phase matching. After the mixing stage the laser beam in addition had to pass several dispersive optics, e.g., dichroitic mirrors and prisms, in order to separate the DFG light from the remaining blue and infrared parts. Regarding those limitations we expected rather low output power of the DFG light of just a few mW. Keeping in mind the pulsed structure of the laser light with a duty cycle of 10^{-3} this value should nevertheless ensure saturation of all reasonably strong optical transitions under our experimental conditions.

B. Atomic beam unit MABU

The atomic spectroscopy, mass separation, and detection of the sodium ions were performed in the atomic beam unit MABU. This machine is a low-energy mass spectrometer with an extraction field of well below 10 V/mm. For chemical decomposition of the sample molecule $NaHCO_3$, reduction and final atomization, a microscopic sample of a few mg was placed in a resistively heated graphite furnace with a diameter of 2.2 mm and a length of 50 mm. The laser beams were directed into the atomic vapor, which formed inside the hot cavity, to induce resonant multistep excitation of the sodium atoms into Rydberg levels, from which they ionize through collisions, black-body radiation from the heated furnace, as well as influences from the electric extraction field. Field ionization of Rydberg atoms is rather strong, but in our case gives only small contributions due to the low tension applied in the extraction region of our apparatus. The individual strengths of the remaining processes cannot easily be disentangled. After acceleration and beam shaping, the ions were guided through an electrostatic 90° quadrupole deflector to remove background from neutral species and a radio-frequency quadrupole mass filter to isolate ^{23}Na from other disturbing masses. Subsequently the highly isotopic pure ion beam was detected by an off-axis-mounted channel electron multiplier in single-ion counting operation.

III. RESULTS

A. Difference frequency generation

One of the two lasers necessary for DFG operated in its fundamental wavelength regime at a wavelength of 920 nm with an average output power of 2500 mW (idler). The second laser operated at 718 nm with 2900 mW and was externally frequency doubled using a BBO crystal cut at 32.8° for type I phase matching (pump). We achieved 700 mW in the blue spectral range around at 359 nm. The light was collimated, separated from the remaining fundamental light, and then focused together with the infrared light into another BBO crystal for DFG. Here, we also implemented type I phase matching at a BBO angle of 32°, which means that both the infrared idler wave and the DFG wave were in ordinary polarization (o) while the frequency-doubled pump light was introduced as an extraordinary (e) wave ($oo \rightarrow e$). After its generation, the DFG light was collimated and separated from the remaining idler and pump parts by a combination of different dichroitic mirrors and dispersive prisms, primarily to allow for power determination. With this simplified setup we obtained up to 11 mW of average power for the DFG light at 589 nm in good agreement with the expectations from the calculations. The overall conversion efficiency is $I_{\mathrm{DFG}}/(I_{\mathrm{idler}} + I_{\mathrm{pump}}) = 0.3\ \%$, which may be increased by using, e.g., the type II phase matching with a BBO suitably cut at 41.5° [12]. Due to the high transition strength of the sodium D lines, less than 2 mW of the DFG light were used for most of the spectroscopic measurements.

For the DFG laser radiation a linewidth (FWHM) of

$$\begin{aligned}\Delta\nu_{\mathrm{DFG}} &= \sqrt{\Delta\nu_{\mathrm{fund}}^2 + \Delta\nu_{\mathrm{SHG}}^2} \\ &= \sqrt{\Delta\nu_{\mathrm{fund}}^2 + (\sqrt{2}\Delta\nu_{\mathrm{fund}})^2} \\ &\approx 6.9(17)\ \mathrm{GHz} \end{aligned} \quad (1)$$

is expected, as only Gaussian contributions determine the width. The range of spectral coverage was not investigated because this is strongly dependent on the available crystals for DFG, which were not optimum during this study. With a set of four properly cut BBO crystals the range of $520 - 680$ nm should be easily accessible by DFG of our Ti:sapphire lasers. Access to the remaining gap of $450 - 520$ nm will require frequency tripling or quadrupling for the DFG pump wave, which will severely complicate the process and reduce the achievable output power.

B. Two-step excitation into the $3d\ 2D_J$ configuration

The three-step excitation scheme used in this work is shown in Fig. 2. It is based on the energy levels as given in [13]. The DFG process was used for the first transition, from the ground state $3s\ ^2S_{1/2}$ to either the level $3p\ ^2P_{1/2}$ at $16956.170\,\mathrm{cm}^{-1}$ (via the D_1 line of the doublet) or to level $3p\ ^2P_{3/2}$ at $16973.366\,\mathrm{cm}^{-1}$ (via D_2). The second transition is induced by a Ti:sapphire laser in fundamental mode to the levels $3d\ ^2D_{3/2,5/2}$ at $29172.887\,\mathrm{cm}^{-1}$ and $29172.837\,\mathrm{cm}^{-1}$, respectively, regarding the selection rule of $\Delta J = \pm 1,0$. However, these two second excited levels are very close lying ($\Delta\nu \approx 1.5$ GHz) and due to the laser linewidth of $3 - 5$ GHz,

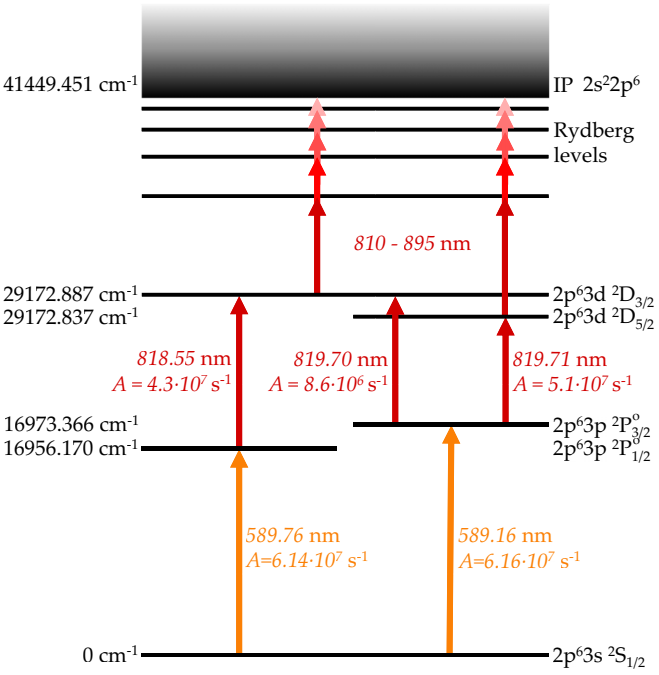

FIG. 2. Sodium excitation schemes investigated in this work. The energy level positions are taken from [13]. The lowest transition on the left side is classically denoted as the D_1 line, the right one as the D_2 line.

they were not resolved when scanning the laser frequency across the second transition. Thus, it was assumed that in the D_2 scheme the majority of the atoms were excited by the stronger transitions to the $J = 5/2$, according to the A factors in the excitation scheme of Fig. 2. For the data analysis, the energetic position of the second excited level during the D_2 excitation was set to a properly weighted intermediate value between the two fine structure sublevels.

To verify the energy position of the two first and second excited states and to get information about the bandwidth of the individual excitation steps, frequency scans on the different transitions were performed while the third step laser was tuned to above the IP for nonresonant ionization. Due to its single valence electron, the spectrum of sodium just above the IP is completely unstructured. Correspondingly, in the third step, no autoionizing state is accessible with our laser system and for excitation into the continuum no resonance structure was observed.

Figure 3 shows on the left the binned frequency scans for the first and second excitation steps of the right excitation ladder of Fig. 2 along the D_2 line and the saturation curves on the right side for all three transitions.

As expected, the saturation power of the first excitation step of 1.1(3) mW, as measured under our experimental conditions, is very low and the transition is easily saturated. The just slightly higher saturation power of 2.6(5) mW for the second step is also well expected due to a comparable oscillator strength as given in Fig. 2; the factor of 2 increase may even be ascribed to an imperfect spatial overlapping of the laser beams. Due to the different contributing broadening effects, a Voigt profile was fitted to the data points of the frequency

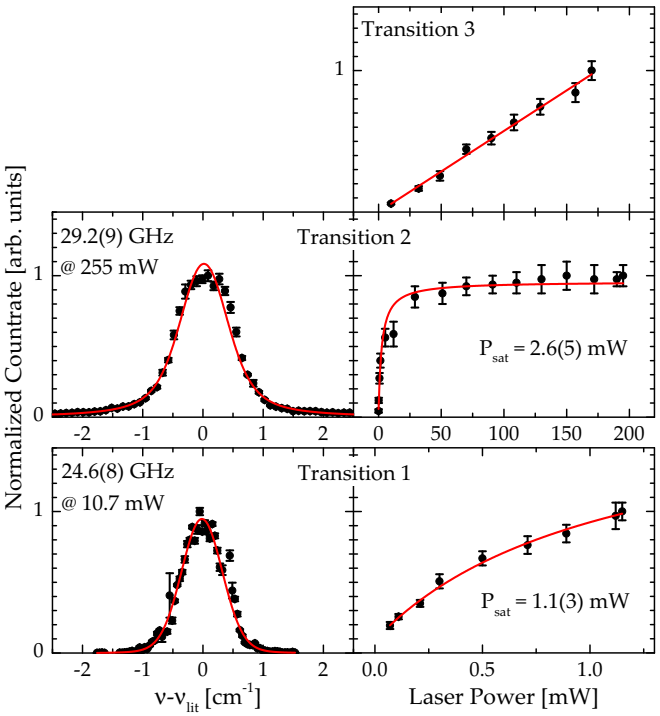

FIG. 3. Frequency scans and saturation curves of the three transitions of the excitation scheme via the D_2 line. Since the third step is nonresonantly ionizing, the resonance curve was omitted and the saturation curve has a constant slope. The extracted linewidths are noted in the graphs.

scans:

$$I(\nu) = A + B\frac{2\ln(2)}{\pi^{3/2}}\frac{\Delta\nu_L}{\Delta\nu_G^2} \times \int_{-\infty}^{\infty} \frac{\exp(-t^2)}{\left(\sqrt{\ln 2}\frac{\Delta\nu_L}{\Delta\nu_G}\right)^2 + \left(\sqrt{4\ln 2}\frac{\nu-\nu_{center}}{\Delta\nu_G} - t\right)^2} dt, \quad (2)$$

where $\Delta\nu_G$ and $\Delta\nu_L$ give the linewidths of the Gaussian and the Lorentzian contribution, respectively. The flattened top of the peak which results from the saturation is not included in the fit model. Nevertheless, the curves perfectly reproduce the outer wings of the peaks, which contain the most important information for the precise extraction of energy positions ν_{center} and FWHM $\Delta\nu$, as obtained using the numerical method given in [14] by

$$\Delta\nu = 0.5346\Delta\nu_L + \sqrt{0.2166\Delta\nu_L^2 + \Delta\nu_G^2}. \quad (3)$$

For the saturation powers P_{sat}, as quoted, a fit function with the form

$$I(P) = A + B\frac{P}{P + P_{sat}} \quad (4)$$

was applied to all three saturation curves. For the nonresonant ionization step an absolutely linear behavior was observed, as expected, for laser powers of up to 175 mW.

C. Linewidths and saturation

For the experimental linewidth of the transitions, we have to consider several contributions. Aside from the negligible natural linewidth (FWHM) of 9.8 MHz for the first step excitation [15] most of the broadening effects contribute in the GHz range. The minimal measured linewidth is limited by the laser linewidth given above. Besides this the Doppler broadening (FWHM) was taken into account with

$$\Delta\nu_{dop} = \frac{\nu_0}{c}\sqrt{\frac{8kT\ln 2}{m_{atom}}} = 2.5(1)\ \text{GHz}, \quad (5)$$

for a frequency of the transition of $\nu_0 = 508.8487$ THz, temperature in the hot furnace of $T \approx 1100$ K, as extrapolated from a pyrometric measurement, and the sodium mass $m_{atom} = 23$ u. The overall Gaussian contribution considers the linewidth of the DFG laser and the Doppler broadening, which is a small contribution due to the low oven temperatures:

$$\Delta\nu_G = \sqrt{\Delta\nu_{DFG}^2 + \Delta\nu_{dop}^2} = 7(2)\ \text{GHz}. \quad (6)$$

The saturation broadening can be approximated by a Lorentzian distribution and gives a significant contribution to the overall linewidth at a maximum laser power of 10.7(10) mW. It is calculated as (FWHM)

$$\Delta\nu_L = \Delta\nu_G\sqrt{1 + S_0} = 24(6)\ \text{GHz}, \quad (7)$$

where $\Delta\nu_G$ is the Gaussian contribution FWHM of the transition and $S_0 = \frac{I}{I_{sat}} = 10(3)$, with laser intensity I and saturation intensity of the transition I_{sat}. For combining Gaussian and Lorentzian contributions we used Eq. (3) with a resulting overall Voigt profile linewidth of the transition of

$$\Delta\nu_{calc} = 26(3)\ \text{GHz}. \quad (8)$$

For the second transition the same calculation with adapted parameters leads to a linewidth expectation of

$$32(5)\ \text{GHz}, \quad (9)$$

where the saturation parameter $S_0 = \frac{I}{I_{sat}} \times 10 = 48(14)$ must additionally be scaled by the saturation of the first excitation step. Notice that there is no additional contribution from the excitation of the pair of energy levels in that step, because this is fully covered by the five times larger laser linewidth.

The calculated linewidths of the two lower excitation steps reproduce the experimental values rather well. When addressing higher spectral resolutions, there are several ways to reduce the linewidths. The biggest contribution results from the large oversaturation, which easily is compensated for by adjusting the intensities of the lasers accordingly. The part resulting from the laser linewidth itself is more complicated to address and would require, e.g., the use of an injection locked system or alternatively a further passive wavelength selection within the laser resonator as discussed, e.g., in [6].

D. Rydberg spectroscopy

For the spectroscopy on sodium Rydberg levels, the laser for the third excitation step was continuously scanned using the wide-range tunable, grating-assisted Ti:sapphire laser to cover the energy range just below the literature value for

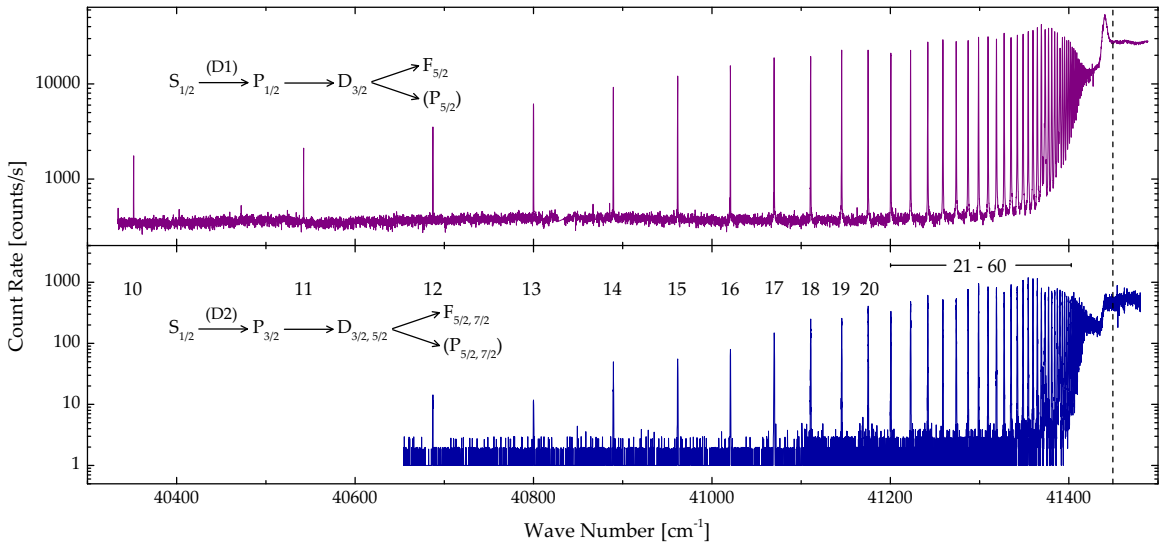

FIG. 4. Two examples of frequency scans of the third step for sodium resonance ionization via the D_1 transition (upper graph) and the D_2 transition (lower graph) as the first step. The excitation scheme and the principal quantum numbers of the determined states are indicated. It should be mentioned that the significant difference in the count rates of the two scans is due to variations in experimental conditions, i.e., settings of the ion optics, and not related to individual transition strengths.

the ionization potential of $E_{\mathrm{IP}}^{\mathrm{lit}} = 41449.451(2)\,\mathrm{cm}^{-1}$ [7,8]. A range of $E_{\mathrm{start}} \approx 40300\,\mathrm{cm}^{-1}$ to $E_{\mathrm{end}} \approx 41500\,\mathrm{cm}^{-1}$ of overall excitation energy was used in the case of the excitation via the D_1 and a slightly narrower range for the D_2 transition. Figure 4 shows representative scans for both schemes in logarithmic scale, where the investigated Rydberg states are numbered according to their principal quantum numbers and $E_{\mathrm{IP}}^{\mathrm{lit}}$ is marked with a dashed line.

We identified Rydberg states of the f series with principal quantum numbers from $n = 10$ to $n = 60$ for the excitation via D_1 and from $n = 12$ to $n = 59$ for the excitation via D_2. Only peaks of one Rydberg series, i.e., belonging to the unresolved $nf\ ^2F^o_{5/2,7/2}$, is visible. This is due to the very low transition strengths into the p series, which is three to four orders of magnitude lower than that into the f states according to [16]. The peaks in Fig. 4 show typical linewidths of $15 - 24$ GHz, which are slightly lower than the linewidth obtained in the frequency scans in Fig. 3 due to the avoidance of strong oversaturation in any of the three consecutive excitation steps during these measurements.

Several scans, upward and downward in energy, were averaged for both excitation schemes. The energy positions found with excitation via both the D_1 line and D_2 line are in a good agreement and perfectly overlap within the statistical error bars. It should be mentioned that the measured deviation for the first ten levels is with $0.09\,\mathrm{cm}^{-1}$ in average larger than for the rest of the levels with a deviation of only $0.03\,\mathrm{cm}^{-1}$ in average. This is due to the count rate, which was in the D_2 scan very low for the first ten peaks. This results in very few data points in each of those peaks, which occasionally led to a shifted energy position in the fit. The fitted and error weighted average energy positions for each Rydberg peak are listed together with the available high-precision literature data from [13] and the most recent data from [9] in Table I. This table also gives the quantum defects calculated with Eqs. (10) and (11) for each Rydberg level.

The statistical error of each level energy consists of the statistical readout error of the wave meter, the uncertainty of the fitted position and a very small error, which accounts for the correction of systematical shifts in wave numbers by the data acquisition system when scanning upward or downward. A systematic error of $0.007\,\mathrm{cm}^{-1}$, which is the $1\,\sigma$ absolute accuracy of the wavelength meter (High Finesse WS6-600), was added afterward to each value. This systematic shift is only applied once, because for the first and second excitation step the literature values, not the herein measured ones, were used for calculation of the total energy. The data in Table I are in perfect agreement with the earlier literature values for nine lower lying levels but slightly disagree for the two cases of $n = 15$ and $n = 19$. The minor discrepancies of 0.05 and $0.03\,\mathrm{cm}^{-1}$, respectively, are well below the uncertainty of the recent measurement of [9] and only slightly exceed the statistical uncertainty of our data, while being covered by the total error. It is thus ascribed to the fact that the literature values from $n = 15$ to $n = 20$ are not measured but calculated using interpolation. Further details of this approach are given in [17], which is the reference quoted in [13]. The data used for the interpolation was taken from [18,19]. Possibly the uncertainties given therein were also somewhat underestimated. In addition, we considered shifts caused by the Autler-Townes effect (ac Stark effect) [20] to be responsible for deviating level energies. In multistep resonance ionization, highly intense light fields can cause a broadening and a splitting of energy levels in the range of several GHz [21]. If the frequencies of the exiting lasers are furthermore detuned regarding the resonance frequencies, an asymmetry of the split structure can occur. In our case, none of the measured peaks are apparently broadened or split which is ascribed to relatively low laser intensities in the interaction region in comparison to those in [21]. Moreover, we set the lasers always at the resonance frequencies, so that only a symmetrical splitting could occur, which would not shift the

TABLE I. Energetic positions (in cm^{-1}) and quantum defects of the measured Rydberg levels of the *f* series together with literature values from [13,9]. The values marked with ^{*a} were used as bandheads for the Rydberg-Ritz fitting routine, those marked with ^{*b} were only interpolated according to [17].

Configuration	Ref. [13]	Ref. [9]	Weighted average	Quantum defect $\delta(n)$
$2p^6 4f$	34586.92(2)^{*a}			
$2p^6 5f$	37057.65(2)^{*a}			
$2p^6 6f$	38399.79(2)^{*a}			
$2p^6 7f$	39208.98(2)^{*a}			
$2p^6 8f$	39734.16(2)^{*a}			
$2p^6 9f$	40094.19(2)^{*a}			
$2p^6 10f$	40351.761(2)		$40351.751(21)_{stat}(7)_{sys}$	0.0016(1)
$2p^6 11f$	40542.293(2)		$40542.293(21)_{stat}(7)_{sys}$	0.0016(1)
$2p^6 12f$	40687.203(2)	40687.19(20)	$40687.193(26)_{stat}(7)_{sys}$	0.0017(2)
$2p^6 13f$	40799.974(2)	40799.92(20)	$40799.964(26)_{stat}(7)_{sys}$	0.0017(2)
$2p^6 14f$	40889.452(2)	40889.39(20)	$40889.438(26)_{stat}(7)_{sys}$	0.0018(3)
$2p^6 15f$	40961.637(2)^{*b}	40961.52(20)	$40961.588(26)_{stat}(7)_{sys}$	0.0024(3)
$2p^6 16f$	41020.714(2)^{*b}	41020.69(20)	$41020.707(26)_{stat}(7)_{sys}$	0.0018(4)
$2p^6 17f$	41069.674(2)^{*b}	41069.62(20)	$41069.662(26)_{stat}(7)_{sys}$	0.0019(5)
$2p^6 18f$	41110.703(2)^{*b}	41110.65(20)	$41110.692(15)_{stat}(7)_{sys}$	0.0020(4)
$2p^6 19f$	41145.425(2)^{*b}	41145.44(20)	$41145.454(15)_{stat}(7)_{sys}$	0.0008(5)
$2p^6 20f$	41175.070(2)^{*b}	41174.98(20)	$41175.067(15)_{stat}(7)_{sys}$	0.0019(6)
$2p^6 21f$		41200.56(20)	$41200.576(15)_{stat}(7)_{sys}$	0.0020(6)
$2p^6 22f$		41222.59(20)	$41222.669(15)_{stat}(7)_{sys}$	0.0030(7)
$2p^6 23f$		41241.95(20)	$41241.980(15)_{stat}(7)_{sys}$	0.0021(8)
$2p^6 24f$		41258.89(20)	$41258.912(15)_{stat}(7)_{sys}$	0.0020(10)
$2p^6 25f$		41273.80(20)	$41273.825(15)_{stat}(7)_{sys}$	0.0039(11)
$2p^6 26f$		41286.91(20)	$41287.083(15)_{stat}(7)_{sys}$	0.0034(12)
$2p^6 27f$		41298.76(20)	$41298.880(15)_{stat}(7)_{sys}$	0.0043(14)
$2p^6 28f$		41309.40(20)	$41309.473(15)_{stat}(7)_{sys}$	0.0015(15)
$2p^6 29f$		41318.89(20)	$41318.919(15)_{stat}(7)_{sys}$	0.0061(17)
$2p^6 30f$		41327.41(20)	$41327.512(15)_{stat}(7)_{sys}$	0.0020(19)
$2p^6 31f$		41335.14(20)	$41335.246(15)_{stat}(7)_{sys}$	0.0029(21)
$2p^6 32f$		41342.20(20)	$41342.283(15)_{stat}(7)_{sys}$	0.0015(23)
$2p^6 33f$		41348.67(20)	$41348.682(15)_{stat}(7)_{sys}$	0.0011(25)
$2p^6 34f$		41354.48(20)	$41354.507(15)_{stat}(7)_{sys}$	0.0040(27)
$2p^6 35f$		41359.77(20)	$41359.867(15)_{stat}(7)_{sys}$	0.0018(30)
$2p^6 36f$		41364.71(20)	$41364.764(15)_{stat}(7)_{sys}$	0.0041(32)
$2p^6 37f$		41369.22(20)	$41369.264(15)_{stat}(7)_{sys}$	0.0080(35)
$2p^6 38f$		41373.43(20)	$41373.490(15)_{stat}(7)_{sys}$	−0.0071(38)
$2p^6 39f$		41377.20(20)	$41377.332(15)_{stat}(7)_{sys}$	−0.0061(41)
$2p^6 40f$		41380.81(20)	$41380.861(15)_{stat}(7)_{sys}$	0.0029(44)
$2p^6 41f$		41384.12(20)	$41384.204(15)_{stat}(7)_{sys}$	−0.0088(48)
$2p^6 42f$		41387.16(20)	$41387.196(15)_{stat}(7)_{sys}$	0.0174(51)
$2p^6 43f$		41390.06(20)	$41390.158(18)_{stat}(7)_{sys}$	−0.0182(65)
$2p^6 44f$		41392.71(20)	$41392.813(18)_{stat}(7)_{sys}$	−0.0151(70)
$2p^6 45f$		41395.22(20)	$41395.280(18)_{stat}(7)_{sys}$	−0.0060(75)
$2p^6 46f$		41397.53(20)	$41397.615(18)_{stat}(7)_{sys}$	−0.0082(80)
$2p^6 47f$		41399.71(20)	$41399.788(18)_{stat}(7)_{sys}$	−0.0042(85)
$2p^6 48f$		41401.75(20)	$41401.831(18)_{stat}(7)_{sys}$	−0.0019(91)
$2p^6 49f$		41403.66(20)	$41403.763(18)_{stat}(7)_{sys}$	−0.0061(97)
$2p^6 50f$		41405.47(20)	$41405.577(18)_{stat}(7)_{sys}$	−0.0090(103)
$2p^6 51f$		41407.18(20)	$41407.253(18)_{stat}(7)_{sys}$	0.0082(109)
$2p^6 52f$			$41408.912(18)_{stat}(7)_{sys}$	−0.0248(115)
$2p^6 53f$			$41410.417(18)_{stat}(7)_{sys}$	−0.0182(122)
$2p^6 54f$			$41411.821(18)_{stat}(7)_{sys}$	0.0019(129)
$2p^6 55f$			$41413.189(18)_{stat}(7)_{sys}$	−0.0075(137)
$2p^6 56f$			$41414.495(18)_{stat}(7)_{sys}$	−0.0254(144)

TABLE I. (*Continued*.)

Configuration	Ref. [13]	Ref. [9]	Weighted average	Quantum defect $\delta(n)$
$2p^6 57f$			$41415.675(18)_{stat}(7)_{sys}$	0.0049(152)
$2p^6 58f$			$41416.859(18)_{stat}(7)_{sys}$	−0.0209(160)
$2p^6 59f$			$41417.944(18)_{stat}(7)_{sys}$	−0.0112(169)
$2p^6 60f$			$41418.982(25)_{stat}(7)_{sys}$	−0.0118(248)

center of the symmetrical fit function applied to the observed data.

To extract the ionization potential from the energy positions, the Rydberg-Ritz formula

$$E(n) = E_{IP} - R_M \frac{1}{n^{*2}}, \tag{10}$$

with the reduced-mass Rydberg constant R_M and the effective quantum number n^* as given by the principal quantum number n and the Ritz expansion of the quantum defect $\delta(n)$ in second order

$$n^* = n - \delta(n) = n - \left(A + B\frac{1}{(n-A)^2}\right), \tag{11}$$

was fitted to the data points as shown in Fig. 5. This graph, with residuals well below 0.05 cm^{-1}, is a representative plot for the different fits, which were also performed individually for the series with excitation via D_1 and D_2, respectively.

Since the peak positions for lower principal quantum numbers could not be measured experimentally in this work, we included the literature values for $n = 4$ to $n = 9$ as bandheads for the fit. This enables a better convergence of the fit, especially regarding the uncertainties of the A and B parameters of the Rydberg-Ritz expansion.

The fit parameters and their uncertainties are given individually for both excitation schemes in Table II. For comparison also the parameters for a fit ignoring the bandheads are included. The variation in the IP values between the two approaches for analysis are truly minor and do not significantly exceed the statistical error bars, while the much lower precision in the A and particularly the B parameters is obvious when omitting the bandheads. The corresponding distortion in the Rydberg-Ritz function even accidentally compensates for the slight discrepancy of 0.023 cm^{-1} obtained between the two excitation schemes by inclusion of the data from [13]. Nevertheless, for both series, via D_1 and D_2, the energy of the average IP value matches the literature value of $E_{IP}^{lit} = 41449.451(2)\,cm^{-1}$ perfectly even within the statistical uncertainties. The trend of the values indicates the possibility that they are systematically shifted by about $\pm 0.007\,cm^{-1}$, which fully confirms the quoted uncertainty of our measurement. Correspondingly, we give the average of both measurements obtained with the inclusion of bandheads as our final value for the first ionization potential of sodium:

$$E_{IP} = 41449.455(6)_{stat}(7)_{sys}\ cm^{-1}.$$

This value is in good agreement with the literature value. The statistical uncertainty given accounts for the fit error which covers all errors in the energy positions of the experimental peaks addressed by the fit. On top of that a systematic error was added as discussed before.

Figure 6 shows the quantum defects for the f series in dependence of the effective quantum number n^*. Similar to that visible in the residuals of Fig. 5, in Fig. 6 minor irregularities are observed in the range of $38 \leqslant n \leqslant 44$. In that range an underlying peak structure which is also well visible in the base line of Fig. 4 but could not be identified, seemingly affects the peak positions and the fitting procedure. The situation is shown in detail in the magnification given in Fig. 7. Nevertheless, the additional peaks observed around $n = 38$ and $n = 43$ have no significant influence on the fit results for the IP.

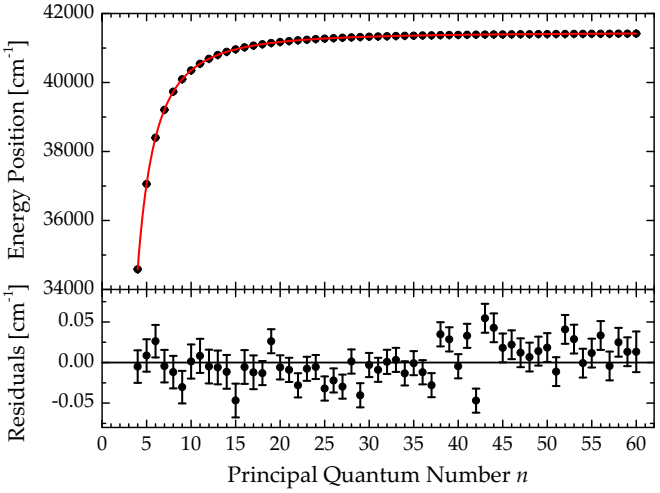

FIG. 5. Energy positions of the Rydberg peaks in dependence of the principal quantum number. The Rydberg-Ritz formula was fitted to the data (red curve). The resulting residuals are given in the lower graph.

TABLE II. Fit parameters for the Rydberg-Ritz fits of the different series. The literature value is from [7,8].

		With bandheads	Without bandheads
D_1	E_{IP} [cm^{-1}]	$41449.443(5)_{stat}(7)_{sys}$	$41449.456(6)_{stat}(7)_{sys}$
	A	0.00169(3)	0.0030(4)
	B	−0.0079(6)	−0.153(45)
D_2	E_{IP} [cm^{-1}]	$41449.466(3)_{stat}(7)_{sys}$	$41449.463(6)_{stat}(7)_{sys}$
	A	0.00172(2)	0.0011(9)
	B	−0.0083(3)	−0.068(240)
Avg.	E_{IP} [cm^{-1}]	$41449.455(6)_{stat}(7)_{sys}$	$41449.460(8)_{stat}(7)_{sys}$
Lit.	E_{IP} [cm^{-1}]	41449.451(2)	

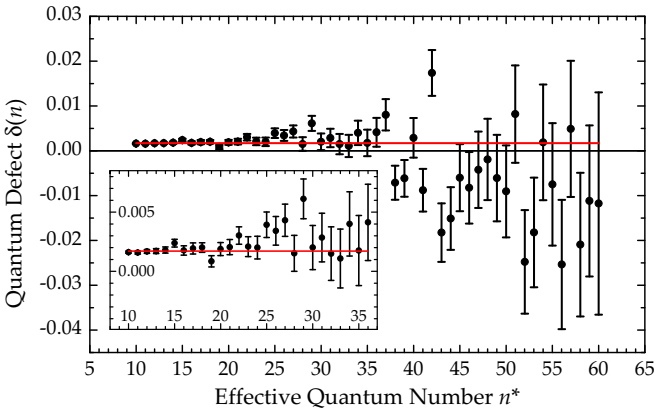

FIG. 6. Quantum defects of the Rydberg levels of the f series measured. The defects were calculated from the measured IP and the energy positions of the resonances. The red curve shows the error weighted average for the quantum defect of $\bar{\delta}(n) = 0.0017(1)$.

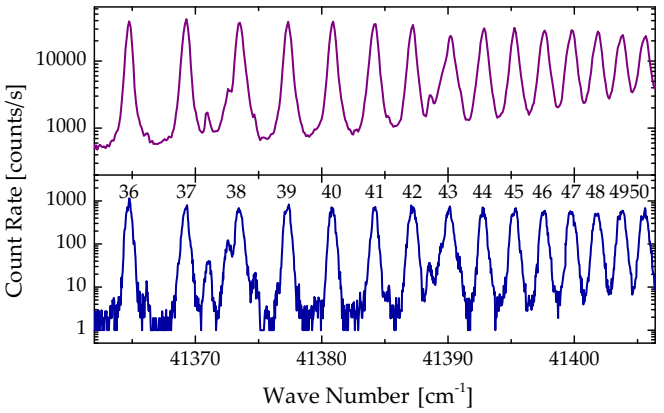

FIG. 7. Enlarged view of the wide range scans in Fig. 4 from $n = 36$ to $n = 50$. In this region an underlying peak structure slightly affects the energy positions of the Rydberg peaks. Excitation in the upper graph via D_1, in the lower via D_2.

IV. CONCLUSION AND OUTLOOK

A. Difference frequency generation

We showed that a laser system based upon the Mainz Ti:sapphire lasers including a DFG stage is ready for midresolution atomic spectroscopy on excitation schemes and high-lying atomic levels and is particularly well suited for operation in the frame of laser ion sources of on-line RIB facilities. Although the present output power of the DFG stage of only about 10 mW is already suitable for reasonably strong first-step transitions, it is still possible to increase this value with simple methods as discussed above, e.g., by involving intracavity frequency doubling for generation of the DFG pump wave. For optimum performance of such a system suitable mixing crystals must be used to deliver a truly significant gain in output power and beam profile. In addition the bandwidth can be lowered to about 50 MHz by using more narrow-band linewidth laser radiation for the fundamental and the frequency-doubled input lasers for DFG. Additionally, this will result in a higher spectral power density and therefore increase the output power.

B. Rydberg spectroscopy of sodium

Using the DFG system discussed above, we performed spectroscopic measurements on the odd-parity Rydberg series $nf\ ^2F^o_{5/2,7/2}$ of sodium. By three-step resonance ionization using excitation schemes via the well-known D_1 and D_2 lines of sodium, we determined the energetic position of 41 high-lying Rydberg states with a high precision of about $0.03\,\mathrm{cm}^{-1}$. We confirmed the already precisely measured first ionization potential of sodium with a precision of $0.02\,\mathrm{cm}^{-1}$ in order to demonstrate the accuracy of our system and the spectroscopic method of in-source multistep resonance ionization spectroscopy, which is becoming more and more popular at on-line laser ion sources.

A minor, so far unexplained finding is the appearance of unexpected humps in the count rate, seen particularly well pronounced in the third step scans in Fig. 4 at approximately $41440\,\mathrm{cm}^{-1}$, just very shortly below the IP. This hump appears in all recorded scans, but has not been observed in other spectroscopic measurement of any of the various elements studied by Ti:sapphire laser resonance ionization so far. It appears sometimes more or less pronounced, which might be ascribed to the conditions of the extraction field being responsible for additional ionization slightly below the IP. This aspect will be investigated systematically in the near future.

ACKNOWLEDGMENTS

J.M.-S. thanks the German Academic Exchange Service (DAAD) for support in the framework of the IAESTE program. P.N. gratefully thanks the Carl Zeiss Stiftung for financial support.

[1] Y. B. Band, C. Radzewicz, and J. S. Krasinski, Phys. Rev. A **49**, 517 (1994).
[2] D. Georgiev, V. P. Gapontsev, A. G. Dronov, M. Y. Vyatkin, A. B. Rulkov, S. V. Popov, and J. R. Taylor, Opt. Express **13**, 6772 (2005).
[3] J. C. Bienfang, C. A. Denman, B. W. Grime, P. D. Hillman, G. T. Moore, and J. M. Telle, Opt. Lett. **28**, 2219 (2003).
[4] W. R. Bosenberg, W. S. Pelouch, and C. L. Tang, Appl. Phys. Lett. **55**, 1952 (1989).
[5] T. W. Hänsch, Appl. Opt. **11**, 895 (1972).
[6] V. Sonnenschein, I. D. Moore, I. Pohjalainen, M. Reponen, S. Rothe, and K. Wendt, JPS Conf. Proc. **6**, 030126 (2015).
[7] M. Ciocca, C. E. Burkhardt, J. J. Leventhal, and T. Bergeman, Phys. Rev. A **45**, 4720 (1992).
[8] J. F. Baugh, C. E. Burkhardt, J. J. Leventhal, and T. Bergeman, Phys. Rev. A **58**, 1585 (1998).
[9] A. Nadeem, M. Shah, S. Shahzada, M. Ahmed, and S. U. Haq, J. Appl. Spectrosc. **82**, 719 (2015).
[10] S. Rothe, B. A. Marsh, C. Mattolat, V. N. Fedosseev, and K. Wendt, J. Phys.: Conf. Ser. **312**, 052020 (2011).

[11] A. Teigelhöfer, P. Bricault, O. Chachkova, M. Gillner, J. Lassen, J. P. Lavoie, R. Li, J. Meiner, W. Neu, and K. D. A. Wendt, Hyperfine Interact. **196**, 161 (2010).
[12] A. V. Smith, Proc. SPIE **4972**, 50 (2003).
[13] J. E. Sansonetti, J. Phys. Chem. Ref. Data **37**, 1659 (2008).
[14] J. J. Olivero and R. L. Longbothum, J. Quant. Spectrosc. Radiat. Transfer **17**, 233 (1977).
[15] C. W. Oates, K. R. Vogel, and J. L. Hall, Phys. Rev. Lett. **76**, 2866 (1996).
[16] *NIST Atomic Spectra Database*, URL http://physics.nist.gov/PhysRefData/ASD/lines_form.html (2015).
[17] S. Dyubko, V. Efremov, S. Podnos, X. Sun, and K. B. MacAdam, J. Phys. B **30**, 2345 (1997).
[18] X. Sun and K. B. MacAdam, Phys. Rev. A **49**, 2453 (1994).
[19] N. H. Tran, H. B. van Linden vanden Heuvell, R. Kachru, and T. F. Gallagher, Phys. Rev. A **30**, 2097 (1984).
[20] S. H. Autler and C. H. Townes, Phys. Rev. **100**, 703 (1955).
[21] S. E. Moody and M. Lambropoulos, Phys. Rev. A **15**, 1497 (1977).